In-situ determination of strain during transient burst testing and the temperature dependence of Zircaloy-4 claddings

S.B. Bell[1], K.A. Kane[+1,2], M.J. Ridley[1], B.E. Garrison[3], B.S. Johnston[1], N.A. Capps[3]
[1]Materials Science and Technology Division, Oak Ridge National Laboratory, Oak Ridge, TN
[2]John Hopkins University Applied Physics Laboratory, Laurel, MD
[3]Nuclear Energy and Fuel Cycle Division, Oak Ridge National Laboratory, Oak Ridge, TN
[+]Formerly at Oak Ridge National Laboratory

ABSTRACT

Understanding fuel system behavior during postulated loss-of-coolant accidents is pertinent for continued safe and efficient operation of light water reactors, particularly as higher burnups are being pursued and safety margins re-evaluated. Conventional mechanical models for the incumbent Zr alloys typically rely on the assumption that steady-state creep is the dominant fuel cladding response during transient accident conditions. To investigate this assumption, simulated accident burst testing was performed on Zircaloy-4 claddings with balloon behavior measured *in-situ*. Two distinct loading conditions were utilized during burst testing: (1) constant-gas-inventory where pressure was allowed to increase with temperature and (2) constant pressure. *In-situ* strains and strain rates were measured via 2-dimensional digital image correlation techniques and synchronized with temperature to determine deformation dependencies. The temperature dependence of strain rate was characterized by a two segment Arrhenius relationship, with a distinct transition between the high and low temperature/strain regimes. The average activation energy of the lower temperature/strain regime was 328 ± 25 kJ/mol, in agreement with the ~320 kJ/mol used for conventional LOCA models. However, the higher temperature/strain segment, which encompassed most of ballooning, showed increased activation energies as well as a dependence on whether the burst region was in view. For tests that burst away from the camera view, the average high temperature/strain segment activation energy was 635 ±150 kJ/mol. For samples where the rupture opening formed in view, the average activation energy was 1015 ± 179 kJ/mol. This observed shift in temperature dependence indicates a transition in deformation mechanism at the end of life, possibly to time independent failure mechanisms, which has not yet been visualized in the literature for Zr alloys. Parameters at the transition points were analyzed to determine thresholds for this change in behavior, which occurred at an average hoop strain of 6.9 ± 2.1 %.

INTRODUCTION

Postulated design-basis accident scenarios in LWRs, such as a LOCA, subject nuclear fuel cladding materials to rapid thermal transients, dynamic internal loading, and high temperature steam environments. During the transient, the Zr claddings could balloon and burst as a result of the internal gas pressure (Helium and fission gas). The nuclear community has long utilized “burst testing” as a means of assessing fuel cladding performance under accident conditions. The two prominent forms of burst testing are: (1) transient heating testing where pressurized claddings are heated at a specified heating rate [1–5] and (2) more conventional isothermal creep, constant loading burst testing [6–8]. Within transient testing (1), two additional subtypes of experiments are found: (a) constant pressure testing where cladding samples are connected to a fixed pressure reservoir [3] and (b) constant-gas-inventory testing where the amount of gas present in the rod is fixed and pressure is allowed to vary with temperature [1,2]. Constant pressure testing simplifies the loading condition and subsequent analysis while a constant gas inventory is more proto-typic of pressure conditions during an accident transient.

Conventional modeling efforts of Zr cladding burst behavior assume steady-state creep is dominant [3,9–12]. This assumption is a reasonable basis, as thermal creep rates for Zr alloys are significantly higher than other material concepts such as Fe-based alloys [13–15]. While LOCA transients subject claddings to inherently non-steady state conditions, application of power law creep has yielded reasonable results in historic [3,9] and modern efforts [12,13,16]. Current creep models assume the creep rate follows a power-law form with an Arrhenius temperature dependence. A general expression of the power-law description for effective strain rate is given by,

$$\dot{\varepsilon}_{eff} = A_{eff}\sigma_{eff}^{n}e^{\frac{-Q}{RT}}, \qquad \text{Eq. 1}$$

where $\dot{\varepsilon}_{eff}$ (s^{-1}) is the effective strain rate, A_{eff} ($MPa^{-n}s^{-1}$) is the structure constant, n is the stress exponent, σ_{eff} (MPa) is the effective stress, Q (J/mol) is the activation energy, R (J/mol-K) is the gas constant, and T (K) is the absolute temperature. Such parameters are determined from traditional constant temperature and load creep testing [6,17].

The stress exponent for Zircaloy-4 (Zry-4) for LOCA relevant creep testing in the α-phase is found in the range of 4.94 – 5.89 [3,6,9,17]. Activation energies used in conventional LOCA models [3,9,11] are ~300 kJ/mol, in relative agreement with the self-diffusion activation energy [18] of Zr. If the Arrhenius temperature dependence explicit in the steady creep LOCA models is accurate, real-time strain deformation data prior to and during ballooning should provide useful for model validation. More specifically, it should be possible to extract a consistent, Arrhenius temperature dependence of strain rate.

Confirmation of this temperature dependence necessitates simultaneous measurement of strain, temperature, and pressure with time throughout the transient. Historic LOCA testing has typically focused on *ex-situ* parameters and failure criteria, i.e., end-of-life metrics. Relevant parameters such as burst pressure, burst temperature, rupture opening size, and post-test diametric strain have been critical for code validation and supporting safety basis. However, *in-situ* strain measurements are needed to refine material models and understanding, particularly relevant for assessing advances in LWR operational efficiency and safety.

Extension of burnup levels beyond a peak rod average burnup of 62 GWd/MTU is currently being pursued in the United States to increase the economic viability of nuclear power plants by extending fuel cycle lengths and reduce batch reload quantities [19]. With higher burnup levels, severe degradation of the fuel pellets during a transient may occur [19,20], leading to concerns of fuel fragmentation, relocation, and dispersal. Rod internal pressures are expected to be higher, increasing the possibility of cladding failure in the low-temperature (< 808 °C) anisotropic α-Zr phase [21,22], rather than the mixed α + β or pure β phase regions. As such, refinement of current LOCA models in the α-phase is necessary for reliably assessing safety concerns related to high burnup extension.

In this work, transient burst testing of Zry-4, both constant-gas-inventory and constant pressure conditions, focused on higher internal pressures that ensured failure in the α phase (≥ 6.2 MPa) was conducted with the application of 2D digital image correlation (DIC). DIC is an increasingly popular experimental strain measurement technique [23,24], and recently, DIC has been used to assess cladding behavior during burst testing across the nuclear community [25–27]. It should be noted that some of the testing in this manuscript has been previously presented [12,27,28], but analysis is expanded to provide insight into the temperature dependence of Zry-4. Additionally, burst testing was performed recently by Ridley et al. [29] with similar analysis as the present manuscript, yet utilizing stereo-DIC.

Furthermore, a framework for model development and validation of cladding behavior offers the opportunity to rapidly accelerate qualification of cladding-fuel forms beyond incumbent systems. This methodology has explicit value for new accident tolerant fuel claddings and could reduce testing needs for developing cladding concepts as a single test generates a statistically significant amount of data.

EXPERIMENTAL METHODS

Transient burst testing in an air environment was conducted on stress-relieved annealed Zry-4 cladding segments using the Severe Accident Test Station (SATS) at Oak Ridge National Laboratory. The claddings had a nominal ingot chemistry of Zr-1.5wt.%Sn-0.2%Fe-0.1%Cr. The as-received outer diameter and wall-thickness of 9.5 mm and 0.575 mm, respectively. Shortened cladding segments (7.62 cm) were utilized in this work to ensure cladding burst occurred in view of the camera system. A 7.62 cm alumina filler rod was placed inside the Zry-4 segments to simulate fuel volume and thermal mass. To maintain cladding train length in the furnace, stainless steel segments with internal filler rods were placed on either side of the cladding and connected by union compression fittings. Further details regarding standard SATS burst testing can be found in previous publications [14,27,30,31].

For this work, a specialized infrared furnace with a 3.8 cm diameter view port in the center was utilized to heat and view the cladding specimens. Testing employed both optical and thermal camera systems, however data from the latter is not presently reported. An Allied Vision GT6600 camera with a 24-megapixel matrix was used to record optical images for 2D DIC. The camera was equipped with a telecentric lens to minimize error associated with out-of-plane motion. An optical mirror was placed in front of the furnace viewport at 45° that reflected light to the DIC camera oriented 90° relative to the furnace view port. A schematic of the furnace is shown in Figure 1(a).

For DIC surface patterning, 0.4 mm squares were laser engraved in columns along the axial direction spaced 0.8 mm apart. The cladding segment was manually rotated 10° between engraving of the columns. The engraving depth for was typically 14-17 um, with a maximum depth of 25 um measured [32]. This equated to ~2.4 – 3% of the nominal wall-thickness. An example of the surface patterning can be found in Figure 1(b).

Due to preliminary investigations into the application of DIC and IR thermography during SATS burst testing, a SiC shell was placed around the cladding segment. The primary purpose of the SiC shell was to eliminate direct reflections from the IR lamps on both optical and IR imaging. The SiC shell also acted as an effective intermediary heat source between the lamps and the cladding due to a high emissivity and thermal conductivity, thus limiting thermal gradients across the sample.

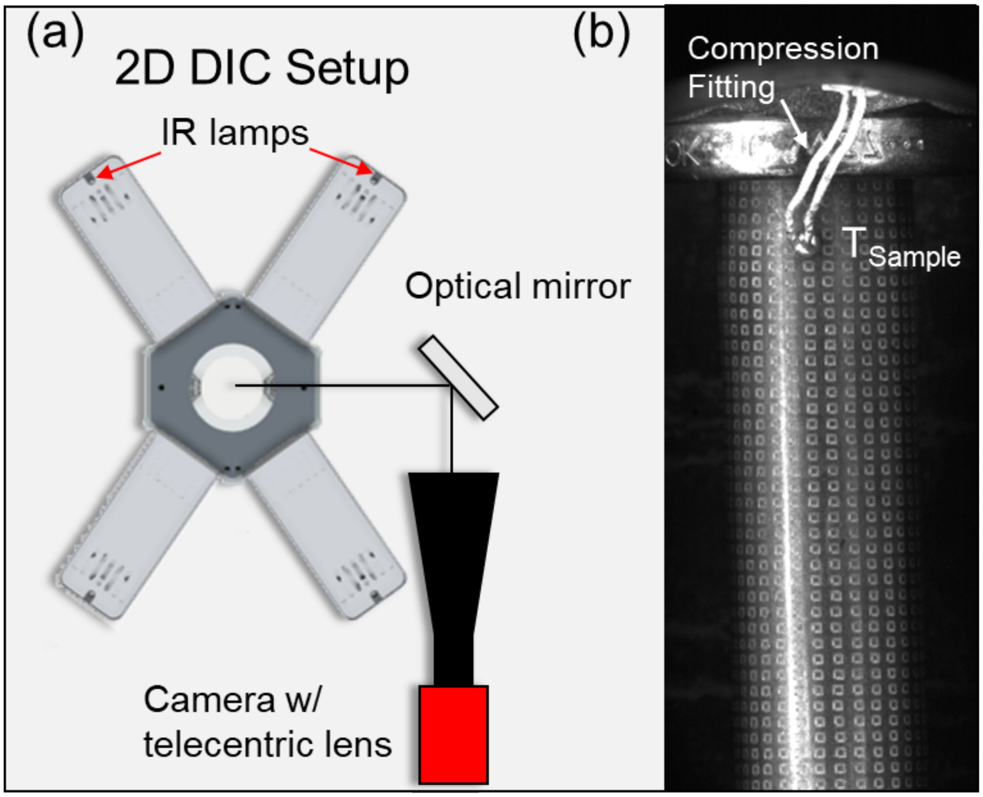

Figure 1. (a) Schematic of the furnace and optical setup. (b) Example image of a laser-engraved specimen.

Eight burst tests in an air environment were completed as part of this work, with internal pressures ranging from 6.2 to 15.1 MPa (Table 1). Two distinct loading conditions were utilized: (a) "open valve" (OV) or constant pressure testing where cladding samples are connected to a fixed pressure reservoir and (b) "closed valve" (CV) or constant-gas-inventory [2] testing where the amount of gas present in the rod is fixed and pressure is allowed to vary with temperature. An OV and CV test was performed at each nominal pressure of 6.2, 8.2, 10.3 and 15.1 MPa, totaling eight tests. When heated to 300 °C before a transient, the initially 15.1 MPa at room temperature (RT) CV test reached internal pressures beyond the current safety limits for SATS. As such, it was depressurized to ~14.8 MPa before the test proceeded.

Three thermocouples (TCs) were present during testing, excluding one test (8.2 MPa CV) as indicated in Table 1. The TC controlling ($T_{Control}$) furnace power output was placed on the Swagelok compression fitting, outside the SiC shell. Another TC (T_{Sample}) was placed 5 mm below the compression fitting and was in view of the DIC camera. The last TC (T_{Back}) was placed in the back of the furnace away from the viewport, 180° from T_{Sample}. Examples of the pressure and temperature histories for an open and closed burst test are shown in Figure 2(a) and Figure 2(b), respectively.

The claddings were initially pressurized at room temperature and heated to 100 °C to confirm no leaks were present. Then the samples were heated to 300 °C at 1°C/s and held for 5 min to ensure stable pressure and furnace conditions were achieved before a transient. After the hold at 300 °C, the claddings were heated at a prescribed rate of 1 °C/s until the claddings failed. The furnace was immediately shut off after burst and the claddings were allowed to air cool. Burst pressure and temperature was recorded and used to provide conventional metrics for comparison to historical models. Burst pressure was determined as the pressure reading before rapid depressurization. Burst temperature was measured using the reading of the TC (front or back) closest to the burst region at the time of failure.

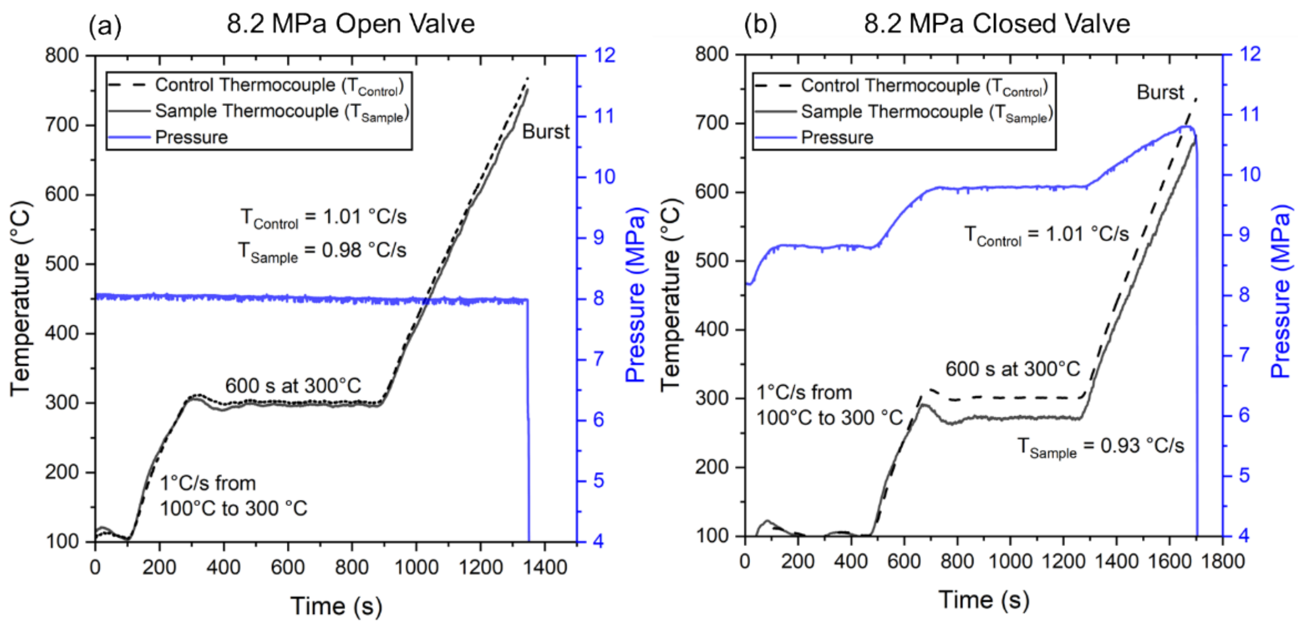

Figure 2. Example temperature and pressure histories for (a) open and (b) closed valve tests.

A linear fit of the temperature histories between the beginning of the ramp and time of burst was performed to determine the heating rate for each test and is presented in Table 1. The average heating rate of all the tests was 0.98 ± 0.05 °C/s, with a maximum and minimum heating rate of 0.92 and 1.08 °C/s, respectively. A heating rate of 1 °C/s was prescribed to the system and generally achieved. The sample temperatures at the start of the ramp also demonstrated variation due to the influence of the SiC shell, which can be observed in Figure 2. The furnace power output during the test was controlled by the TC outside the SiC shell. As such, during the 300 °C hold prior to ramp the TC in view (T_{Sample}) sample was cooler due to the shielding by about 20 – 30 °C for some specimen.

The presented DIC strain data was measured at the center of the balloon region, focused on an approximately planar section to mitigate the influence of out-of-plane rotation. An example of the DIC analysis region on the laser engraved pattern during ballooning is presented in Figure 3. All temperature correlations with DIC data were based on the reading of the TC in view, T_{Sample}. Hoop and axial strain curves presented in this work are raw measurements from an in-house DIC software. Due to systematic noise brought about largely by heat waves in the furnace, all strain curves were smoothed using an adjacent averaging filter before numerical differentiation to determine strain rate.

After testing, a VR-3100 Keyence structured light microscope was utilized for profilometry, imaging, and determination of post-test diametric strain. Lastly, the samples were cross-sectioned at approximately the center of the balloon region and mounted in epoxy. Scanning electron microscopy (SEM) was performed on the samples using a Tescan MIRA3 to investigate oxide formation in the air environment and the laser engraving form.

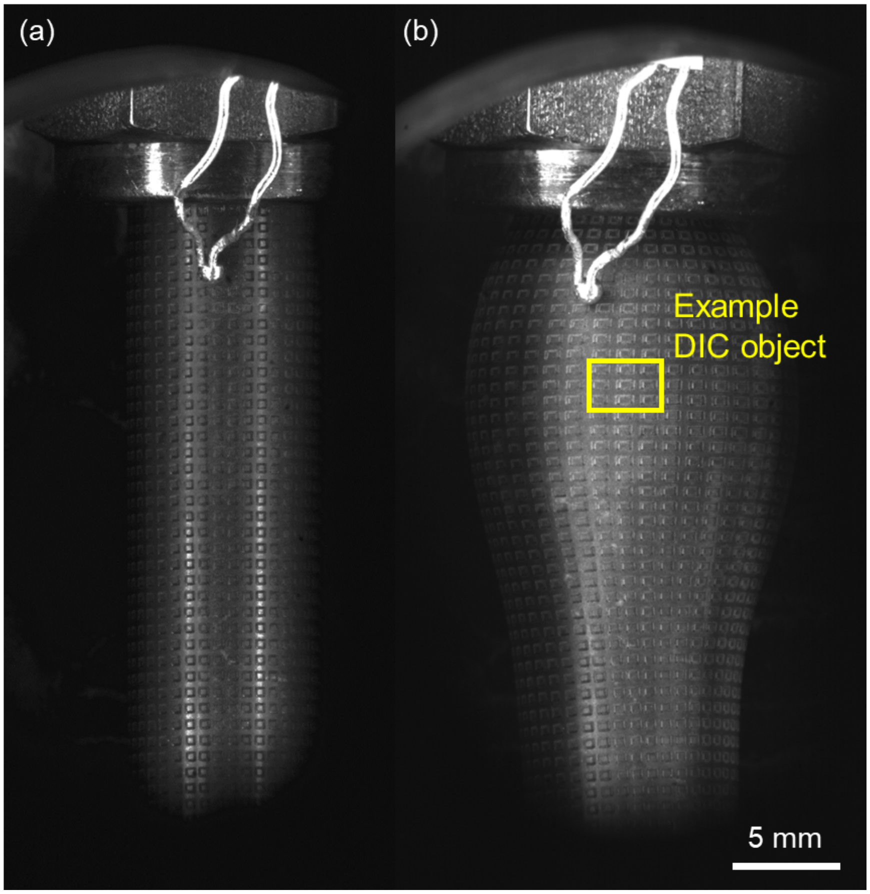

Figure 3. Image of a cladding specimen (a) before ballooning and (b) right before burst. The yellow square encompassing a 3 by 3 grid of laser engraved squares illustrates the location of and subset used for analysis.

Table 1. Test matrix, loading conditions, and burst data for all tests presented in this work. *Sample was repressurized at 300 °C to 14.8 MPa.

Internal pressure at RT (MPa)	Loading Condition (Open/Closed)	Front TC Ramp Rate (°C/s)	Front TC reading (°C)	Back TC reading (°C)	Burst Pressure (MPa)	Burst Location
6.2	Open	1.08	797	833	6.01	Back
6.2	Closed	0.99	738	777	7.63	Back
8.2	Open	0.98	751	761	7.97	Front
8.2	Closed	0.93	682	NA	10.36	Back
10.3	Open	0.92	687	721	10.11	Back
10.3	Closed	0.95	656	680	12.92	Between
15.1	Open	1.03	671	617	14.99	Front

15.1*	Closed	0.96	630	680	15.61	Front

RESULTS

In-situ Strain Comparison

Figure 4(a) and Figure 4(b) display the time-dependent hoop and axial true strain measurements for the OV and CV tests. The tests conducted at pressures of 6.2, 8.2, 10.3, and 15.1 MPa are represented by black, green, blue, and purple lines, respectively. As strain was measured in the center of the balloon region, Figure 3(b), the location of the rupture was important to consider during analysis.

For four of the eight tests, burst occurred on the backside of the furnace away from the camera view. For the 10.3 MPa OV sample burst in between the two TCs, resulting in a rupture opening ~90° away from the camera view. The remaining three samples burst directly in view of the camera, allowing for analysis near or on the burst opening. Figure 5. presents an illustration to provide clarification regarding the relative orientation of the camera and rupture location for further discussions in this manuscript. Figure 5.(a) illustrates the orientation for samples that burst "in-view" of the camera while Figure 5.(b) shows the relative orientation for specimens where rupture occurred "out-of-view" of the camera. Significantly larger strains were observed for the samples that burst in-view of the camera due to the onset of non-uniform strains associated with rupture. As such, samples that burst in-view of the camera are represented by dashed or dotted lines in Figure 4 to distinguish this observation.

Post-test strain in the same analysis region was measured for comparison against DIC using scans of the sample surface. This comparison was not available for samples that burst in-view, as the rupture formed in this region. The post-test measurements for samples burst out-of-view showed agreement within ~2% of the DIC final strain value.

Cladding trains were not rigidly constrained on the bottom end, but loosely bound so to keep the cladding fixed in the center of the furnace. Axial strain was generally found to be negative, with maximum magnitudes of ~2 to 8%. However, for the 8.2 MPa CV and OV tests, Figure 4(a) and Figure 4(b), axial strain rapidly increases near the end of life. A positive final axial strain was measured for the 8.2 MPa OV test (dashed green curve in Figure 4(a)). This could indicate a transition to a state where the axial stress led to a positive deformation rate, as the axial direction is in tension, rather than being dominated by volume considerations from the hoop strain. The remainder of the tests did not demonstrate this behavior.

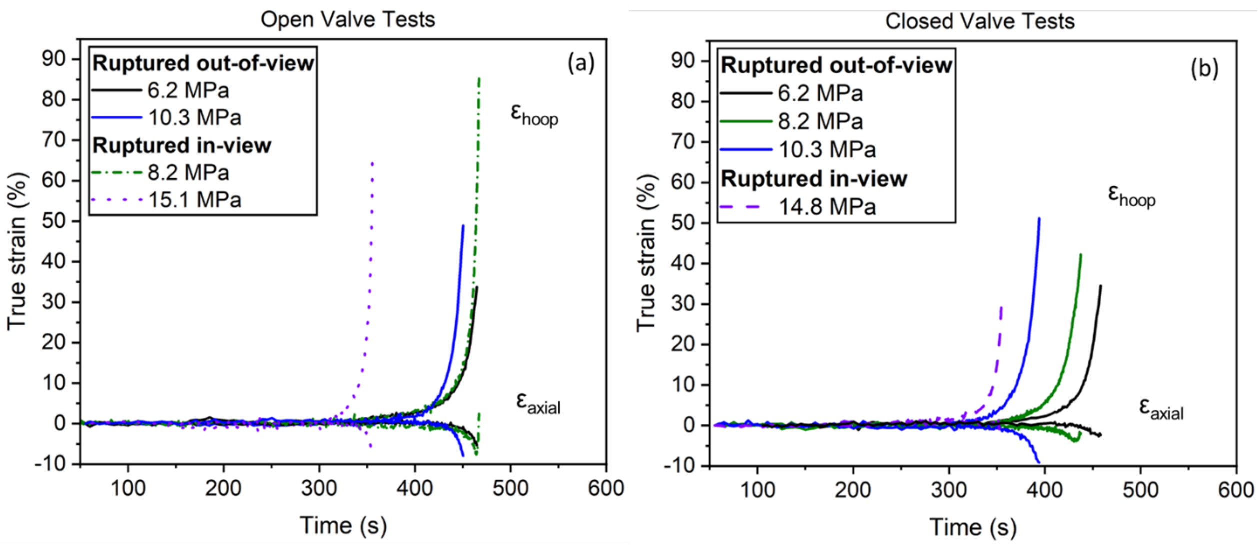

Figure 4. Hoop and axial strain-time curves for the (a) closed valve and (b) open valve tests.

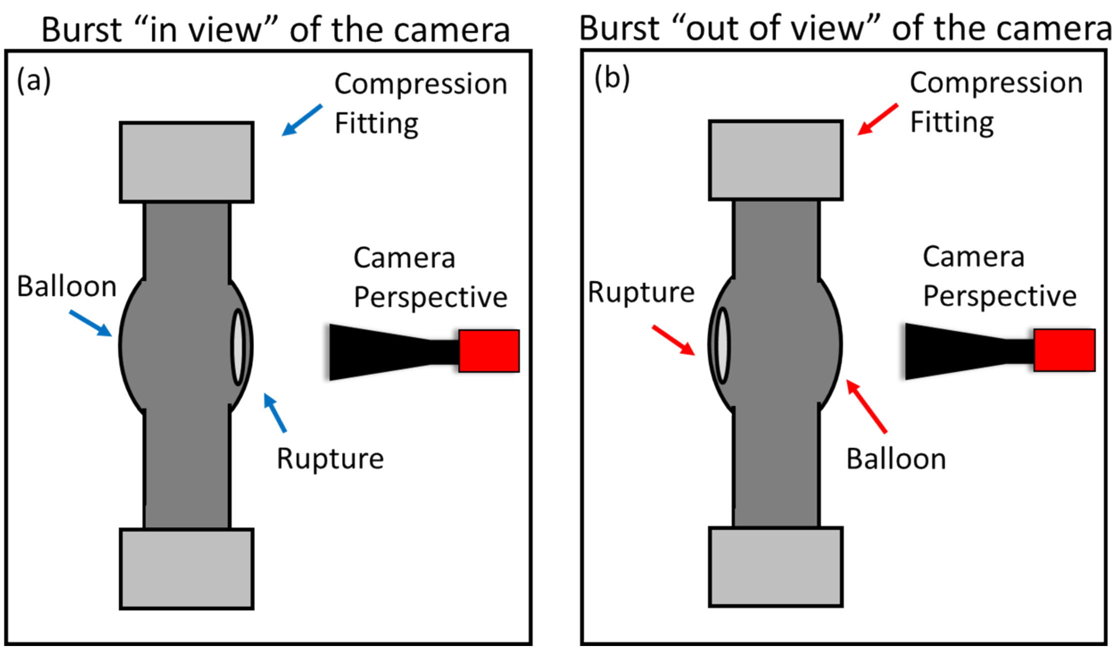

Figure 5. Illustrations of the relative orientations between the rupture opening and camera perspective for (a) specimens that burst “in-view” and (b) “out-of-view” of the camera.

The CV and OV tests were pressurized to the same initial value at RT, however, the readings near the end of life for the CV tests were ~1.5 – 2.5 MPa higher than the OV tests due to the increasing temperature and closed pressure system. As such, direct comparison of the strain curves for different loading conditions with the same initial RT pressure is generally not possible. However, the pressure during ballooning of the 6.2 MPa CV test was comparable to 8.2 MPa OV test.

Hoop strain and pressure for both tests are presented against time from the start of the 1 °C/s ramp in Figure 6. The 6.2 MPa CV and 8.2 MPa OV tests are shown in red and black, respectively. Solid lines represent pressure, and the dashed lines indicate the true hoop strain curves. Stars at the end of the strain curve indicate the final strain values. As the 8.2 MPa OV test burst in view of the camera, the latter portion of the strain measurements were higher due to observation of non-uniform strain associated with rupture. Regardless, the two tests showed considerable overlap particularly during the start of deformation. It should be noted, the two samples also showed a similar overlap when considering strain as a function of temperature.

The onset of ballooning is not clearly definable based on the strain curves. Considering the 6.2 MPa CV test in Figure 6, at ~370 s the rate of pressure change decreased and then leveled off. This pressurization rate change is expected due to volume changes and coincided with the beginning of hoop strain increase. At ~431 s the 6.2 MPa CV test reached a maximum pressure of 7.98 MPa. Comparatively, the OV test was pressurized to 8.00 MPa at the same point in the temperature ramp. It should be noted that a small pressure leak was present for the 8.2 MPa OV test, with a ~0.2 MPa decrease in pressure from the moment of pressurization. At ~431 s into the ramp, the strain curves demonstrated similar hoop strain values of ~7%. After this point, the strain curves diverged. The volume increases due to rapid ballooning for the constant gas inventory test led to a corresponding decrease in pressure until failure occurred. While only the 6.2 MPa CV test pressure history is discussed in detail, the tests with a constant gas inventory showed similar pressurization-strain relations.

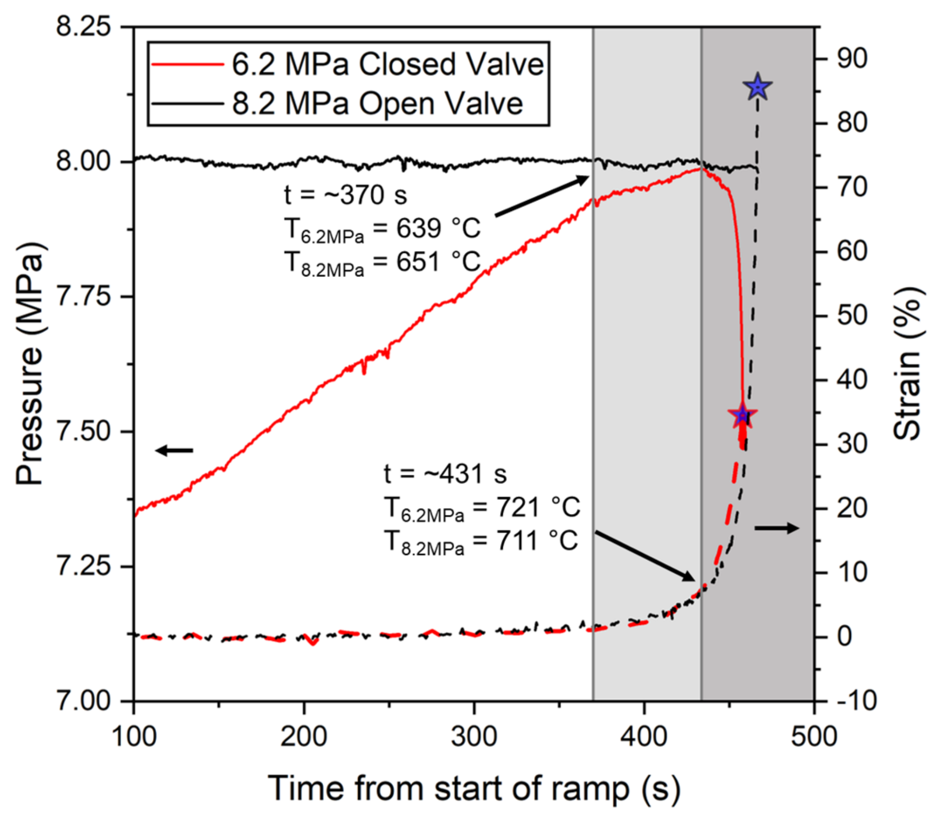

Figure 6. Strain and pressure against time for the 6.2 MPa closed valve and 8.2 MPa open valve tests.

While the curves in Figure 6 provides a valuable comparison between loading conditions, which will be discussed in detail later, consideration of the combined time, i.e., strain rate and temperature relationship is valuable for investigating the Arrhenius temperature dependence assumption. Evaluating the relationship between strain-rate and temperature during a transient is necessary due to the basis of Eq. 1 in LOCA modeling. Strain-rate and temperature dependence are discussed in a later section.

Strain Rates at Failure

Models of cladding performance typically utilize some form of failure criterion to terminate the simulation. A commonly applied "plastic instability" threshold implemented in TRANSURANUS [33] and BISON [11] fuel performance codes indicates failure occurs once an effective strain rate of 2.78 %/s (100 hr^{-1}) is reached. As in, the simulation would be terminated and the deformation at this point considered the end state. To compare this criterion with the *in-situ* data and evaluate possible discrepancies in predictions, the final measured effective and hoop strain rates are presented against burst pressure in Figure 7(a). The effective, or equivalent, plastic strain was calculated using an isotropic assumption given by,

$$\varepsilon_{eff} = \sqrt{\frac{2}{3}\left(\varepsilon_{hoop}^2 + \varepsilon_{axial}^2 + \varepsilon_{radial}^2\right)}, \quad \text{Eq. 2}$$

where ε_{hoop}, ε_{axial}, and ε_{radial} are the strains in the hoop, axial, and radial directions, respectively. The resultant strain curves were then smoothed and numerically differentiated. Given the non-uniform deformation inherent to the burst location, tests where the burst occurred in view of the camera are not discussed.

Final strain rates are also plotted against the reading from the TC in view of the camera (T_{Sample}) in Figure 7(b). The final effective and hoop strain rates are presented in squares and triangles, respectively. Linear fits of both quantities are also presented. As DIC is inherently a surface measurement, radial strain was determined assuming constancy of volume during plastic deformation. It should be noted the α-Zr phase for which testing encompassed is inherently anisotropic due to the hcp crystal structure. A simple isotropic assumption is relevant for a first comparison.

Most of the measured strain rates at failure were greater than the plastic instability criterion of 2.78 %/s. The final effective strain rate was higher than the final hoop strain rate, where the magnitude of difference between the two quantities varied between tests. The largest difference observed between the two was 0.9 %/s for the 8.2 MPa CV test, while the smallest difference of 0.04 %/s was found for the 6.2 MPa CV test. Both final hoop and effective strain rate increased with burst pressure, but the former showed a lower dispersion trend. A decreasing trend was observed for final strain rates and burst temperature with similar dispersion, Figure 7(b). This inverse relationship is expected, as higher pressures are known to result in lower burst temperatures. The slopes of the burst pressure trendlines for the final hoop and effective strain rates data were in relative agreement with 0.322 and 0.360 %/(MPa·s), respectively. A similar relationship was found for temperature with slopes of -0.0149 and -0.0165 %/(°C·s) for the final hoop and effective strain rate trendlines, respectively.

At lower burst pressures and higher temperatures, the final effective strain rates are closest to the described plastic instability criterion of 2.78 %/s. Final effective strain rate values of the 6.2 MPa OV and CV tests were 2.65 and 2.314 %/s, respectively. The remainder of the tests in Figure 7 failed at strain rates higher than the critical value. The 8.2 MPa CV, 10.3 MPa OV, and 10.3 MPa CV samples reached effective strain rates ≥ 2.78%/s at 2, 4, and 4 seconds, respectively, before burst. This corresponds to a difference of 7%, 15%, and 15% effective strain at failure, respectively, beyond where the simulation would have ended.

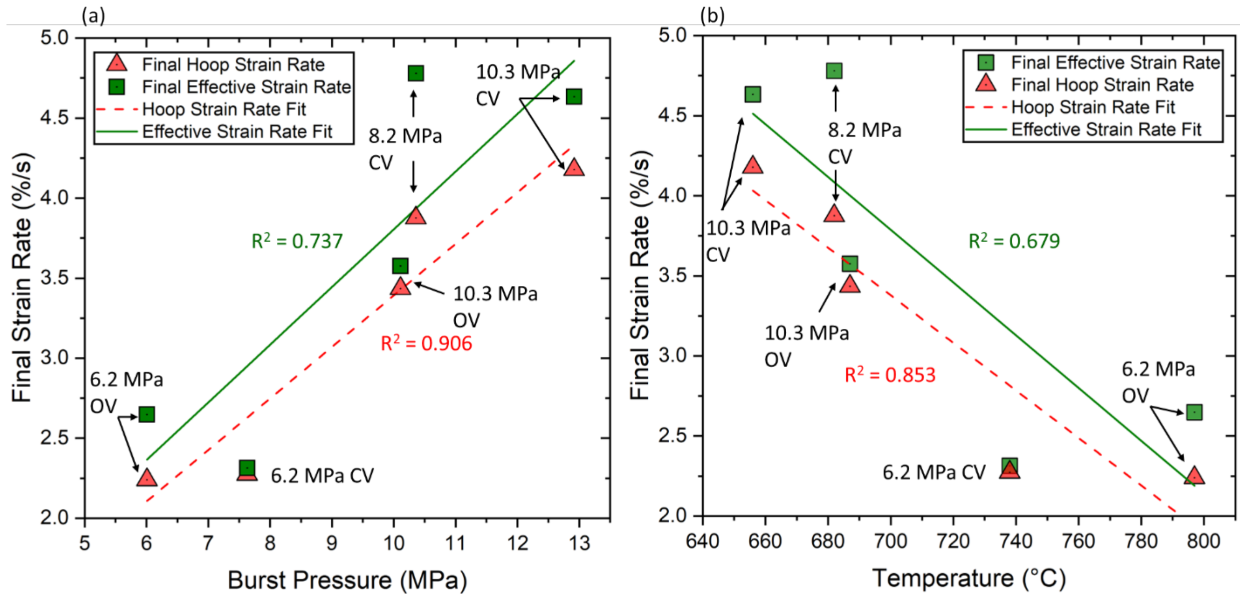

Figure 7. Final hoop and effective strain rates against (a) burst pressure and (b) T_{Sample} reading at burst for tests that burst away from view of the camera. “OV” and “CV” labels in the figure represent open and closed valve tests, respectively.

Ex-situ Strain Comparison

Burst pressure is presented against burst temperature in Figure 8 as well as reported in Table 1. OV and CV tests are shown in squares and triangles, respectively. The average temperature difference between the front and back thermocouples at failure was 35 ± 15 °C. Burst typically occurred near the hottest location, with the rupture forming near the highest reading TC for six of the eight tests. For comparison of this testing against historical data, the empirical Chapman correlation for Zircaloys based on a 1 °C/s heating rate [1,2,34] is included in the black line in Figure 8 . Generally, the burst data aligns with the historical Chapman correlation particularly at lower pressures. For pressures > ~10MPa, a deviation from the correlation is observed. This nonconformity could be due to constraint of the balloon region near the compression fittings that will be described next.

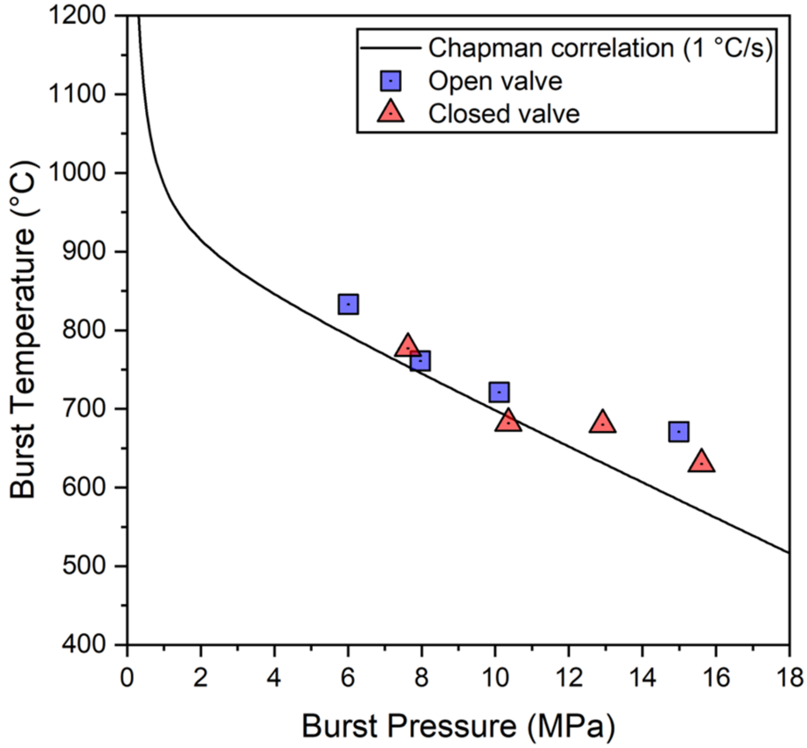

Figure 8. Burst temperature versus pressure data for all tests.

The balloon region formed near the top fitting due to the influence of the SiC shell and the top compression fitting being exposed directly the IR lamps. Images of some of the specimens are presented in Figure 9(a) to demonstrate profile form after testing. To quantitatively illustrate this, post-test diametric strain profiles are presented in Figure 9(b). The profiles were determined using image analysis, by measuring the distance between the edges of the cladding at points along the axial direction. All measurements were conducted with the burst opening perpendicular to the image plane as shown in Figure 9(a), to avoid inclusion of deformation associated with the rupture. OV and CV tests are presented in hollow and solid symbols, respectively. The symbols are divided by nominal fill pressure at RT with the 6.2 MPa, 8.2 MPa, 10.3 MPa, and 15.1 MPa tests are presented in squares, triangles, circles, and diamonds, respectively.

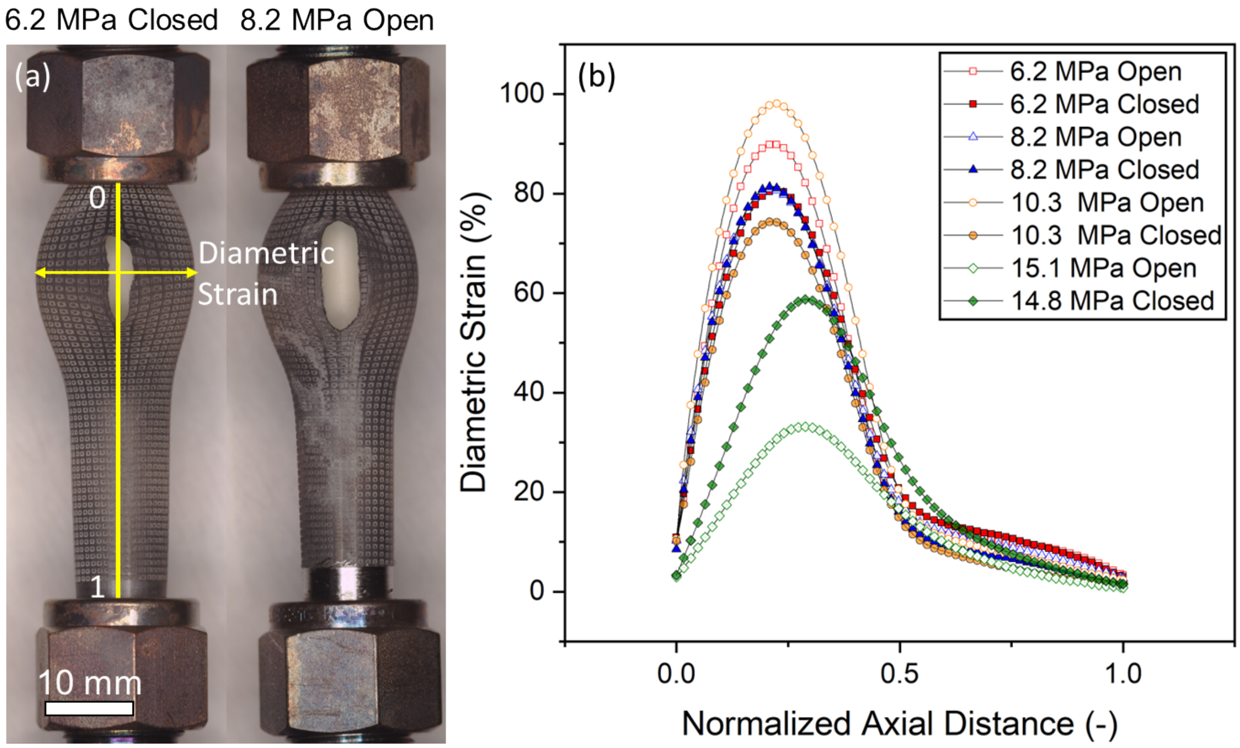

Figure 9. (a) Optical images of the 6.2 MPa closed and 8.2 MPa open valve tests. The double-sided arrow indicates the measurement of the diameter at a given axial point. The line a perpendicular to this represents the axial direction which measurements were performed. The top compression fitting, closer to the balloon region, was defined as zero in the measured profiles. (b) Diametric engineering strain versus normalized distance along the axial direction for all tests.

Comparing again the 6.2 MPa CV and 8.2 MPa OV tests, the post-test strain profiles demonstrated similar form and magnitude. Again, it should be noted that the 8.2 MPa OV test burst in view of the camera, initially overlapping with the 6.2 MPa CV test at lower strain (~431 s, 7% hoop strain) and eventually demonstrating greater strain associated with rupture formation. As such, this indicates the importance of considering view orientation with DIC data, and the disconnection between local and more global strain behavior. It also suggests that the point of divergence may also be when localized non-uniform strain initiates.

However, this association of loading profile with strain does not hold for all *ex-situ* comparisons. For example, the 8.2 MPa CV and OV tests also had similar balloon profiles despite a ~2.39 MPa difference in burst pressure. Notably, the 15.1 MPa nominal pressure samples, Figure 9(b), has considerably lower post-test diametric strains compared to the other tests. It is currently unclear as to why those specific tests burst more towards the center.

From Figure 9, it is evident that the axial balloon geometry is asymmetric for all tests. The portion of the balloon region opposite the top compression fitting (closer to 1) shows a gradual decrease in the strain gradient further away from the balloon peak. However, symmetry is existent on both sides of the balloon region, particularly near the peak of the balloon. To demonstrate this quantitatively, the derivative of diametric strain with respect to the normalized axial profile of the 6.2 MPa OV and CV tests are presented in Figure 10 alongside the strain profiles. For both tests, the derivative profiles showed a linear downtrend from ~0.05 to 0.35 normalized axial distance. The end of the profile closer to 0 shows an increase in the strain gradient before transitioning to this linear segment. This is most likely due to the impingement of the cladding near the compression fitting. Regardless, the linear derivative implies a constant second derivative and a parabolic form to the balloon region. As such symmetry around the peak balloon is observed for some portion of the balloon curve. This observation is relevant, as DIC analysis was performed in the center of ballooning and indicates possibly limited effect of the constraint.

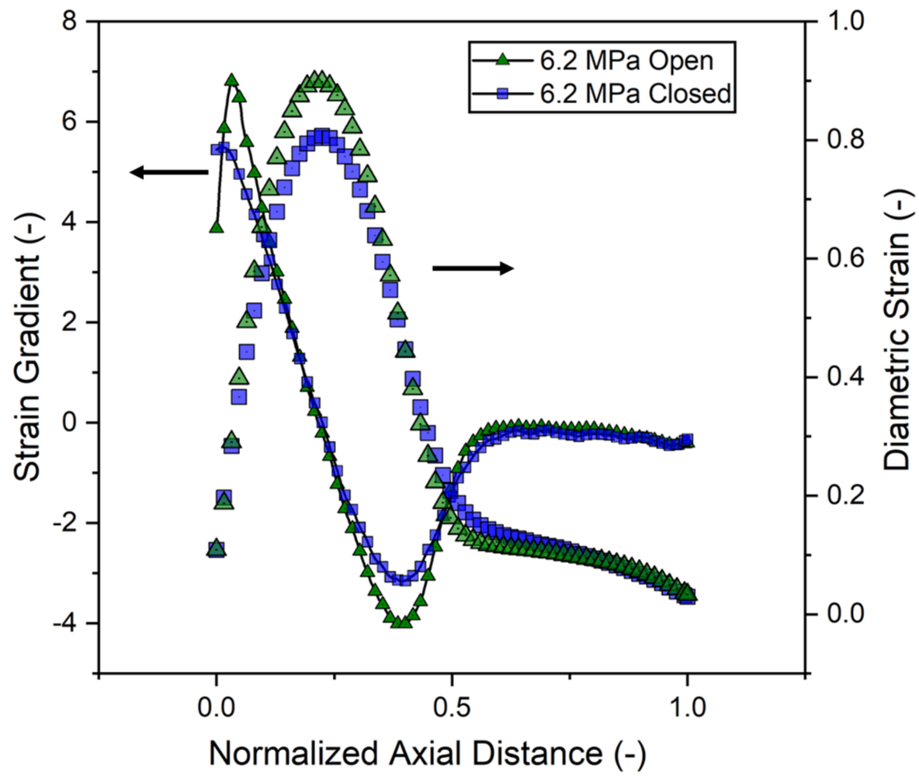

Figure 10. Diametric strain profiles along the axial direction alongside numerical derivatives of those profiles to demonstrate symmetry of the peaks.

Strain Rate and Arrhenius Temperature Dependence

LOCA modeling of Zircaloy claddings often assumes ballooning is primarily driven by steady state creep following a power law form with an Arrhenius temperature dependence, Eq. 1. For a system with an Arrhenius temperature dependence, the inverse temperature and the natural logarithm of strain rate should produce linear relations. In terms of steady-state creep rates this dependence is best shown by reworking Eq. 1,

$$ln(\dot{\varepsilon}) = \ln(A) + n * \ln(\sigma) - \frac{Q}{RT}, \qquad \text{Eq. 3}$$

where the slope of the line is proportional to the activation energy, Q.

To investigate the steady state assumption, Figure 11 and Figure 12 present inverse temperature and the natural logarithm of strain rate in the hoop direction. Whether or not the burst region was in view of the cameras had significant impact on the measured temperature dependence. Samples that burst in view of the camera, i.e., the region of analysis was near or on the rupture location, are discussed separately.

Specimen that burst away from the view of the camera are presented in Figure 11 with the 6.2 MPa OV, 6.2 MPa CV, 8.2 MPa CV, and 10.3 MPa CV tests in hexagons, triangles, diamonds, and circles, respectively. As the 10.3 MPa OV test burst between the front and back thermocouples, it was not included but briefly discussed below. For most of the test, the strain rate was affected by noise due to heat waves. However, towards the end of the test the strain became large enough (~2%) that the effect of the heat waves on the measurement was reduced. Analysis of temperature dependence was performed on data after reaching a true hoop strain of 2% due to this consideration. Similar analysis for axial strain is not presented as the noise was too significant. Regardless, hoop strain measurements were able to provide insight into temperature dependence.

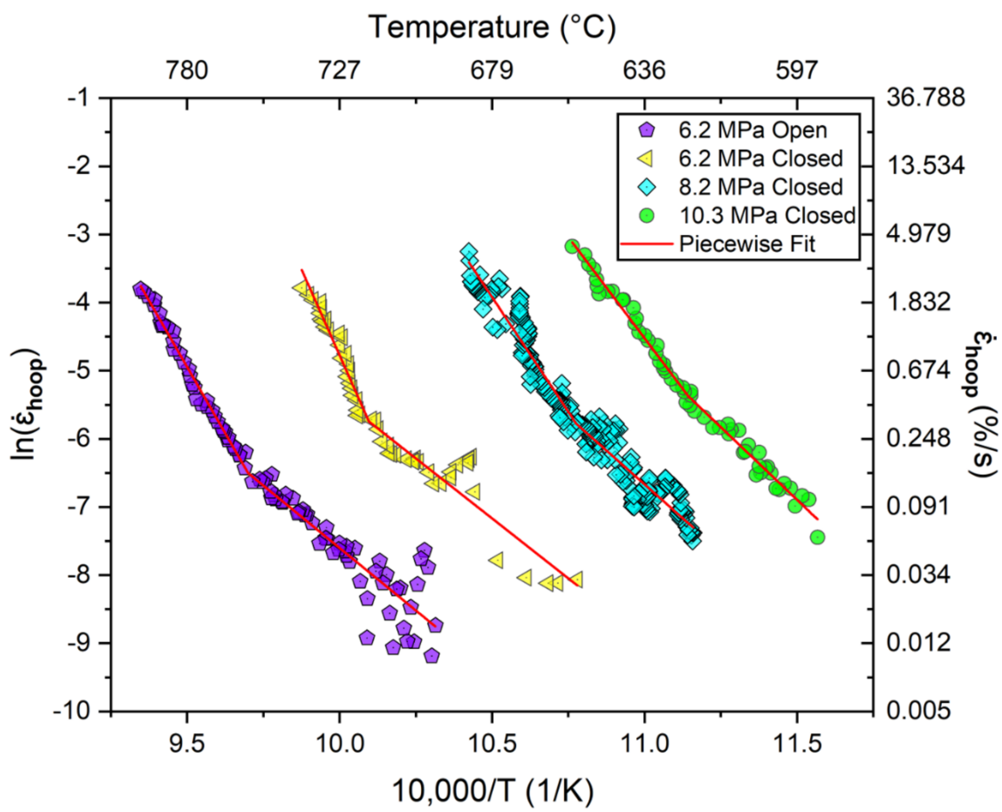

Figure 11. Natural logarithm of strain rate against inverse temperature for the tests that burst away from view of the DIC camera.

Figure 11 shows distinct linear trends are present in the strain rate-temperature data. Two linear regions were observed: (1) a segment which encompassed the earlier parts of the ramp occuring at lower temperatures associated with lower strain/strain rates and (2) a segment encompasing the later portion of deformation at higher temperatures associated with greater strain/strain rates. This behavior suggests a possible a transition in deformation mechanisms. As such, piecewise linear fits consisting of two segments were applied to the curves in Figure 11 using the Levenberg-Marquardt method to quantify these temperature dependencies and the transition point between them. Piecewise fits are shown in red lines in Figure 11. Data determined from temperature dependence analysis is presented in Table 2. The error values in Table 2 represent the standard error of the regression.

The lower temperature segments shown in Figure 11 had slopes, i.e., “activation energies” ranging from 293 – 355 kJ/mol. The average activation energy of the low temperature/strain segment for the tests in Figure 11 was 320 ± 28 kJ/mol. In contrast, the higher temperature/strain linear segments had activation energies of varying from 493 – 840 kJ/mol, with an average value of 635 ± 150 kJ/mol. These observations indicate higher activation energies and greater variation in temperature dependence near the end of life.

Table 2. Activation energies and transition parameters for two segment linear fits.

Sample Name	Low Temperature Q (kJ/mol)	High Temperature Q (kJ/mol)	Strain (%)	Temperature (°C)	Pressure (MPa)	Strain Rate (%/s)
6.2 MPa Open	304 ± 17	647 ± 36	5.27	758	6.04	0.150
6.2 MPa Closed	293 ± 21	840 ± 73	7.09	717	7.98	0.321
8.2 MPa Open	344 ± 18	1076 ± 45	9.91	723	8.00	0.385
8.2 MPa Closed	330 ± 15	560 ± 19	7.18	655	10.8	0.310
10.3 MPa Open	N/A	886 ± 32	N/A	N/A	N/A	NA
10.3 MPa Closed	355 ± 15	493 ± 16	8.12	624	13.76	0.466
15.1 MPa Open	344 ± 29	1156 ± 45	7.77	648	15	0.584
14.8 MPa Closed	31.4 ± 117	813 ± 38	3.05	594	16.1	0.069

Figure 12 shows the temperature dependence for samples where burst occured in view of the DIC camera, i.e., the strain analysis was performed near or at the rupture location. The 8.2 MPa OV, 15.1 MPa OV, and 14.8 MPa CV tests are presented in squares, triangles, and circles, respectively. The 2% strain threshold for analysis was applied to the samples in Figure 12 for consistency.

Two distinct linear segments were found for the 8.2 MPa and 15.1 MPa OV tests, similar to Figure 11. The lower temperature segments resulted in activation energies of 344 ± 18 and 344 ± 29 kJ/mol for the 8.2 MPa and 15.1 MPa OV tests, respectively. Higher temperature segments of those two tests resulted in activation energies of 1076 ± 45 and 1156 ± 45 kJ/mol, respectively.

For the 14.8 MPa CV sample it is possible that a transition is present, but occurred shortly after the qualitative 2% strain threshold. However, looking at Figure 12 a transition at ~600 °C is possible. A piecewise fit was applied to the data for consistency with the other sample analyses and to ensure adequate fitting of the possible higher temperature/strain segment. This resulted in a more objectively determined activation energy at higher temperatures/strains for comparison against the rest of the data set, yet is still subject to caution. The scatter and limited data range present in the lower temperature regime influenced the fit, leading to an implausible activation energy of 31.4 ± 117 kJ/mol. For the high temperature segment, an activation energy of 813 ± 38 kJ/mol was determined. The average activation energy of the high temperature segments for the samples that burst in view was 1015 ± 179 kJ/mol.

Lastly, the 10.3 MPa OV test burst between the front and back of the furnace. Linear behavior was observed for this test above 2% strain, with no apparent transition. As such, a single linear segment was fit to the data, but not presented, resulting in an activation energy of 886 ± 32 kJ/mol. While the low temperature segments displayed activation energies in agreement with creep and historic models, the high temperature segments were unusually high. These values are labeled as "activation energies" due to the method of analysis in this work. It is likely these values are not emblematic of creep activation energy. The high temperature "activation energies" should be treated as apparent values, neccesitating further investigation beyond this dataset.

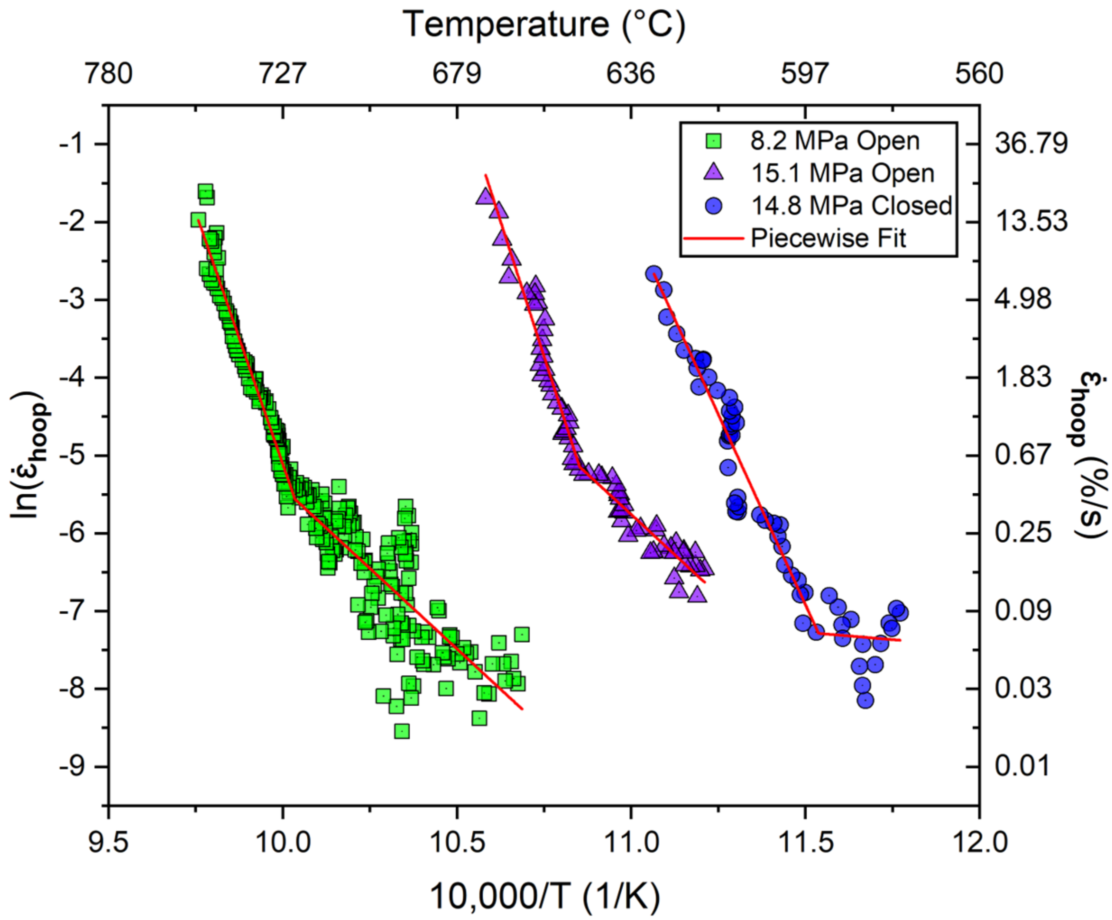

Figure 12. Arrhenius style plots for the tests that burst in view of the camera.

Combining the lower temperature regime values from Figure 11 and Figure 12, excluding the 14.8 MPa CV test, resulted in an average activation energy of 328 ± 25 kJ/mol. This value agrees with the conventional activation energy of ~320 kJ/mol utilized in LOCA models. Considering the average activation energies above for the high temperature segments, there is a strong dependence on which side of the cladding is in view.

The parameters recovered from these fits were analyzed to determine possible criteria for this transition in behavior. The common point for the two segments resulted in the temperature, pressure, strain, and strain rate at the time of the transition, presented in Table 2. From Table 2, it is readily apparent that higher pressures were associated with lower temperatures at the transition point. If there is a transition to another mechanism, it appears to be both temperature and stress dependent. However, all tests that demonstrated the two linear segments transitioned at true hoop strains less than 10%. The average true strain at the transition was 6.9 ± 2.1 %. Similarly, the average strain rate was 0.33 ± 0.17 %/s.

It is important to note the analysis performed in this section did not account for the changing stress state with deformation. Attempts were made to utilize strain meaurements to incorporate changing stress into analysis. The compounding of noise in calculating stress using strain and numerically differentiating strain rendered these attempts unsuccessful. Future work, with refined patterning and experimental methods, is planned to address this gap and provide more detailed investigations.

SEM and Oxide Analysis

A SEM micrograph of the region opposite burst for the 14.8 MPa CV sample after testing is presented in Figure 13(a). A higher magnification micrograph centered on a laser-engraving is presented in Figure 13(b). Looking at Figure 13(b), the engraving structure takes a semi-circle form that is distorted in the hoop direction due to ballooning. After testing, the depth of the laser engravings is on the order of ~20 µm, equivalent to ~4% of the post-test cladding thickness. Due to the testing in an air environment, ZrO_2 formation was found on the outer diameter of all Zircaloy specimens, Figure 13(b). Initial surface roughness in conjunction with the laser engravings led to variation in oxide formation, but in general the oxide thickness was on the order of ~ 1 µm. On either end of the laser-engravings, material was raised compared to the surrounding cladding. This debris oxidized considerably more compared to the material between engravings. As testing was conducted in air, energy dispersive X-ray spectroscopy (EDS) was performed on the oxide to investigate the presence of nitride formation in the scale. EDS point scans revealed that negligible nitrogen was present in the scale, with oxygen and zirconium being predominant.

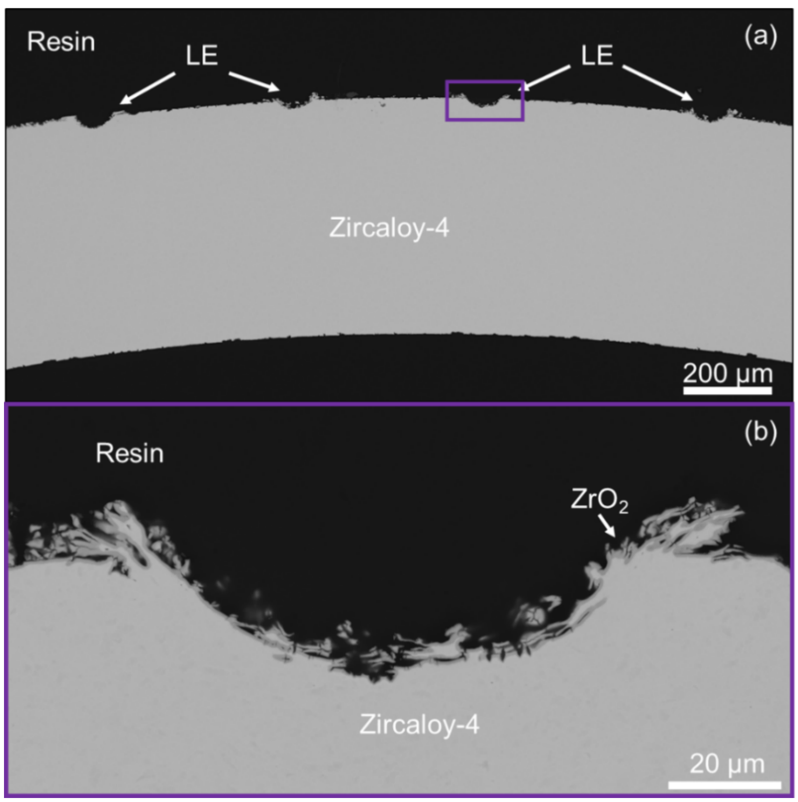

Figure 13. (a) SEM micrograph of the backside of a cladding after testing. (b) Higher magnification micrograph showing the structure of a side of a laser engraving.

DISCUSSION

An Arrhenius temperature dependence was observed for strain in the hoop direction for all tests, Figure 11 and Figure 12. Six of the eight tests presented demonstrated two distinct trends, regardless of whether the rupture location was analyzed (in-view and out-of-view of the camera). Due to the systematic noise described above, the temperature dependence is only distinct for the last ~70-100 °C of the test and when the strain was greater than ~2% true hoop strain. As the tests generally failed at hoop strains of 20 to

60%, these portions account for most of the deformation during testing. Linear fits of the lower temperature/strain segments resulted in an average activation energy of 328 ± 25 kJ/mol. This value is in agreement with the activation energy used in the creep based LOCA model from Erbacher et al. [3] of ~320 kJ/mol for the α-Zr phase.

While the lower temperature/strain segments of behavior gave activation energies near ~320 kJ/mol regardless of whether rupture was in view, the higher temperature/strain segments did not. Claddings that burst out of and in view had an average activation energy of 635 ± 150 and 1015 ± 179 kJ/mol for the higher temperature/strain segment, respectively. This observation demonstrates the importance of considering where on the balloon region analysis is occurring with nodal measurement techniques like DIC. As in, strain rate profiles at azimuthal locations around the cladding could have a range of activation energies in the second high temperature regime. Similarly, it exemplifies the relevance for more nuanced, albeit exceedingly difficult, consideration of the local strain development for modeling efforts. More global *in-situ* characterizations, such as measuring diametric changes, could miss such behavior. Thermal gradients during testing may also contribute to the observed behavior. Historic burst testing [1] efforts have demonstrated the significant influence of azimuthal thermal gradients on the final diametric strain of α-Zr. While strain from DIC analysis can be correlated with a single thermocouple, thermal gradients still need to be considered and investigated further.

It is important to note that the "activation energies" measured from a single transient test are not directly comparable to those obtained from large-scale isothermal creep testing. Analysis of cladding behavior utilized concepts and nomenclature of "activation energies" due to the historic reference frame of secondary creep mechanisms dominating Zr LOCA behavior and the Arrhenius dependence observed between strain rate and temperature. Yet, the *in-situ* observations in this work have demonstrated the validity of such an empirical framework. The transition in temperature dependence supports the prospect of a parameter or mechanism change. In the paradigm of creep deformation, this apparent activation energy increase could be the result of a changing stress exponent, power-law breakdown, or the onset of tertiary creep. Caution must be taken when utilizing insight from conventional time dependent and independent mechanical testing, as in LOCA simulations the transient heating ultimately drives the failure process. The transition in strain rate temperature dependence was interpreted using simplified creep analysis leading to a discussion of a dramatic increase in steady-state creep activation energy, but it is possibly due to the formation of an instability that accelerated deformation and initiated ballooning after material strength limits were reached.

These high temperature/strain segments encompass much of ballooning, a rapid and inherently non-uniform deformation process, similar to that classically associated with specimen behavior after plastic instability and ultimate tensile strength limits are reached in conventional tensile testing. In the context of burst testing, there are two distinct localizations: (1) the nodal and characteristic curvature that shapes the balloon over a substantial portion of the tube, and (2) the shorter scale localized region within the balloon where rupture occurs. A localized instability that forms, (1) may drive the subsequent ballooning process as it seeks stress relief from surrounding material until enough thinning occurs for (2) rupture. Such an instability driven balloon event would explain the viewing dependence for the high temperature/strain activation energies. As in, the instability region would have been analyzed for samples that ruptured in-view, leading to a naturally higher strain rate for a given temperature.

Considering historic models for material strength and the onset of plastic instability, such as Considère's criterion [35] based on maximum load or later extensions to biaxial stress states from Swift [36], may be useful for defining the transition point in deformation behavior. The possible relevance of these criteria was demonstrated by the comparison of loading conditions in Figure 6. At 431 s into the ramp the maximum load/pressure was reached, and hoop strain rapidly increased thereafter for the 6.2 MPa CV test (constant gas inventory). This point corresponded with the transition in temperature dependence for the 6.2 MPa CV test. The stress state at the transition in strain rate temperature dependence relative to the temperature dependent strength of the material will be more adequately assessed in future work, giving further insight into the underlying mechanisms driving ballooning. Reducing noise and systematic errors is crucial in future efforts to investigate this possible relationship. Implementing techniques such as stereo DIC with speckle paint patterns would enhance the quality of the measurements and allow for more nuanced assessment of the balloon region. Additionally, the use of paint for patterning would allow for investigation into coated accident tolerant fuel cladding systems, for which laser engravings would be ill-suited.

CONCLUSIONS

Zircaloy-4 cladding segments were subjected to simulated LOCA transients and 2D-DIC was leveraged to characterize *in-situ* balloon behavior. Arrhenius temperature dependencies for strain rate were observed with two distinct segments indicating a possible change in deformation mechanism. The "low" temperature regime produced activations energies consistent with current LOCA models based on creep parameters. A transition to a greater activation energy was found for the "high" temperature segment. The activation energy of this regime was dependent on the part of the cladding in view during ballooning. For tests where the rupture formed out of and in view of the cladding, the average activation energies of the high temperature segment were 635 ± 150 and 1015 ± 179 kJ/mol, respectively. This observation demonstrates the nuance of cladding behavior that is revealed through techniques like DIC, compared to conventional global measures like diametric strain. Despite this difference in behavior, the transition occurred at an average hoop strain of 6.9 ± 2.1 %, indicating a possible threshold for change in behavior for modeling efforts. Further testing with reduced systematic noise and cladding assemblies free of constraint from the compression fittings is needed to validate and expand upon these findings. Finally, measured strain rates for the samples that burst away from the DIC camera displayed a linear dependence with rupture pressure. At lower burst pressures, final strain rates measured showed relative agreement with a conventional 2.78%/s modeling failure criteria.

ACKNOWLEDGEMENTS

This work was supported through the Advanced Fuels Campaign by the U.S. Department of Energy, Office of Nuclear Energy. The authors would like to express their appreciation to J. Keiser, S. Dryepondt, and C. Massey for providing detailed technical feedback on this manuscript.

CITATIONS

[1] R. Chapman, J. Crowley, A. Longest, G. Hofmann, Zirconium Cladding Deformation in a Steam Environment with Transient Heating, in: J. Schemel, T. Papazoglou (Eds.), Zircon. Nucl. Ind., ASTM International, West Conshohocken, PA, 1979: pp. 393-393–16. https://doi.org/10.1520/STP36692S.

[2] D.A. Powers, R.O. Meyer, Cladding Swelling and Rupture Models for LOCA Analysis, US Nuclear Regulatory Commission, NUREG-0630, 1980.

[3] F. Erbacher, H. Neitzel, H. Rosinger, H. Schmidt, K. Wiehr, Burst Criterion of Zircaloy Fuel Claddings in a Loss-of-Coolant Accident, in: D. Franklin (Ed.), Zircon. Nucl. Ind., ASTM International, West Conshohocken, PA, 1982: pp. 271-271–13. https://doi.org/10.1520/STP37058S.

[4] F. Erbacher, S. Leistikow, Zircaloy Fuel Cladding Behavior in a Loss-of-Coolant Accident: A Review, in: R. Adamson, L. Van Swam (Eds.), Zircon. Nucl. Ind., ASTM International, West Conshohocken, PA, 1987: pp. 451-451–38. https://doi.org/10.1520/STP28138S.

[5] M.E. Markiewicz, F.J. Erbacher, Experiments on Ballooning in Pressurized and Transiently Heated Zircaloy-4 Tubes, Karlsruhe Insititute, KfK 4343, 1988.

[6] A.T. Donaldson, T. Healey, R.A.L. Horwood, Biaxial creep deformation of Zircaloy-4 PWR fuel cladding in the α , (α +β), and β phase temperature range, in: British Nuclear Energy Society, European Nuclear Society Behav, Stratford-upon-Avon, United Kingdom, 1985: pp. 83–89.

[7] S. Leistikow, G. Schanz, Oxidation kinetics and related phenomena of zircaloy-4 fuel cladding exposed to high temperature steam and hydrogen-steam mixtures under PWR accident conditions, Nucl. Eng. Des. 103 (1987) 65–84. https://doi.org/10.1016/0029-5493(87)90286-X.

[8] J. Brachet, M. Dumerval, V. Lezaud-Chaillioux, M. Le Saux, E. Rouesne, D. Hamon, S. Urvoy, T. Guilbert, Q. Houmaire, C. Cobac, G. Nony, J. Rousselot, F. Lomello, F. Schuster, H. Palancher, J. Bischoff, E. Pouillier, Behavior of Chromium Coated M5TM Claddings under LOCA Conditions, in: Water React. Fuel Perform. Meet., Jeju Island, Korea, 2017.

[9] H.E. Rosinger, A model to predict the failure of zircaloy-4 fuel sheathing during postulated LOCA conditions, J. Nucl. Mater. 120 (1984) 41–54. https://doi.org/10.1016/0022-3115(84)90169-7.

[10] T. Manngård, A.R. Massih, Modelling and Simulation of Reactor Fuel Cladding under Loss-of-Coolant Accident Conditions, J. Nucl. Sci. Technol. 48 (2011) 39–49. https://doi.org/10.1080/18811248.2011.9711677.

[11] J.D. Hales, R.L. Williamson, S.R. Novascone, G. Pastore, B.W. Spencer, D.S. Stafford, K.A. Gamble, D.M. Perez, R.J. Gardner, W. Liu, J. Galloway, C. Matthews, C. Unal, N. Carson, BISON Theory Manual: The Equations Behind Nuclear Fuel Analysis, Idaho National Laboratory, INL/EXT-13-29930, 2016.

[12] N. Capps, M. Ridley, Y. Yan, S.B. Bell, K. Kane, BISON Validation to In-situ Cladding Burst Test and High Burnup LOCA Experiments, Ann. of Nucl. Ene. 191 109905 (2023). https://doi.org/10.1016/j.anucene.2023.109905

[13] R. Sweet, N. George, K. Terrani, B. Wirth, BISON Fuel Performance Analysis of FeCrAl cladding with updated properties, Oak Ridge National Laboratory, ORNL/TM-2016/475, 2016.

[14] C.P. Massey, K.A. Terrani, S.N. Dryepondt, B.A. Pint, Cladding burst behavior of Fe-based alloys under LOCA, J. Nucl. Mater. 470 (2016) 128–138. https://doi.org/10.1016/j.jnucmat.2015.12.018.

[15] K.A. Gamble, T. Barani, D. Pizzocri, J.D. Hales, K.A. Terrani, G. Pastore, An investigation of FeCrAl cladding behavior under normal operating and loss of coolant conditions, J. Nucl. Mater. 491 (2017) 55–66. https://doi.org/10.1016/j.jnucmat.2017.04.039.

[16] J. Kim, J.W. Yoon, H. Kim, S.-U. Lee, Prediction of ballooning and burst for nuclear fuel cladding with anisotropic creep modeling during Loss of Coolant Accident (LOCA), Nucl. Eng. Technol. 53 (2021) 3379–3397. https://doi.org/10.1016/j.net.2021.04.020.

[17] H.E. Rosinger, P.C. Bera, W.R. Clendening, Steady-state creep of zircaloy-4 fuel cladding from 940 to 1873 K, J. Nucl. Mater. 82 (1979) 286–297. https://doi.org/10.1016/0022-3115(79)90011-4.

[18] T.A. Hayes, M.E. Kassner, Creep of zirconium and zirconium alloys, Metall. Mater. Trans. A. 37 (2006) 2389–2396. https://doi.org/10.1007/BF02586213.

[19] N. Capps, C. Jensen, F. Cappia, J. Harp, K. Terrani, N. Woolstenhulme, D. Wachs, A Critical Review of High Burnup Fuel Fragmentation, Relocation, and Dispersal under Loss-Of-Coolant Accident Conditions, J. Nucl. Mater. 546 (2021) 152750. https://doi.org/10.1016/j.jnucmat.2020.152750.

[20] J. Cabrera-Salcedo, J. Zhang, G. Khvostov, A. Gorzel, F. Brankov, P. Nagase, P. Raynaud, M. Bales, T. Taurines, A. Nakajima, A. Alvestav, Report on Fuel Fragmentation, Relocation, Dispersal (FFRD), Nuclear Energy Agency, NEA/CSNI/R(2016)16, 2020.

[21] A. Miquet, D. Charquet, C.H. Allibert, Solid state phase equilibria of zircaloy-4 in the temperature range 750–1050°C, J. Nucl. Mater. 105 (1982) 132–141. https://doi.org/10.1016/0022-3115(82)90367-1.

[22] A.R. Massih, Transformation kinetics of zirconium alloys under non-isothermal conditions, J. Nucl. Mater. 384 (2009) 330–335. https://doi.org/10.1016/j.jnucmat.2008.11.033.

[23] H.A. Bruck, S.R. McNeill, M.A. Sutton, W.H. Peters, Digital image correlation using Newton-Raphson method of partial differential correction, Exp. Mech. 29 (1989) 261–267. https://doi.org/10.1007/BF02321405.

[24] M.A. Sutton, J.J. Orteu, H.W. Schreier, Image Correlation for Shape, Motion and Deformation Measurements: Basic Concepts, Theory and Applications, 1st Ed., Springer Verlag-US, 2009.

[25] D. Campello, N. Tardif, J. Desquines, M.-C. Baietto, M. Coret, A. Maynadier, P. Chaudet, Validation of a multimodal set-up for the study of zirconium alloys claddings' behaviour under simulated LOCA conditions, Strain. 54 (2018) e12279. https://doi.org/10.1111/str.12279.

[26] D.-H. Kim, G.-H. Choi, H. Kim, C. Lee, S.-U. Lee, J.-D. Hong, H.-S. Kim, Measurement of Zircaloy-4 cladding tube deformation using a three-dimensional digital image correlation system with internal transient heating and pressurization, Nucl. Eng. Des. 363 (2020) 110662. https://doi.org/10.1016/j.nucengdes.2020.110662.

[27] K. Kane, S. Bell, B. Garrison, M. Ridley, M. Gussev, K. Linton, N. Capps, Quantifying deformation during Zry-4 burst testing: a comparison of BISON and a combined in-situ digital image correlation and infrared thermography method, J. Nucl. Mater. 572 (2022) 154063. https://doi.org/10.1016/j.jnucmat.2022.154063.

[28] K. Kane, B. Garrison, S. Bell, B. Johnston, N. Capps, K. Linton, Report Summarizing Progress in Digital Image Correlation Analysis of Burst Phenomenon, Oak Ridge National Laboratory, ORNL/TM-2022/2382, 2022.

[29] M. Ridley, C. Massey, S. Bell, N. Capps, High temperature creep model development using in-situ 3-D DIC techniques during a simulated LOCA transient, Ann. Nucl. Energy. 193 (2023) 110012. https://doi.org/10.1016/j.anucene.2023.110012.

[30] K. Kane, S. Lee, S. Bell, N. Brown, B.A. Pint, Burst behavior of nuclear grade FeCrAl and Zircaloy-2 fuel cladding under simulated cyclic dryout conditions, J. Nucl. Mater. 539 (2020) 152256. https://doi.org/10.1016/j.jnucmat.2020.152256

[31] S.B. Bell, K.A. Kane, C.P. Massey, L.A. Baldesberger, D. Lutz, B.A. Pint, Strength and rupture geometry of un-irradiated C26M FeCrAl under LOCA burst testing conditions, J. Nucl. Mater. 557 (2021) 153242. https://doi.org/10.1016/j.jnucmat.2021.153242.

[32] K. Kane, N. Capps, B. Garrison, B. Johnston, S. Bell, K. Linton, Development and Implementation of Digital Image Correlation for Out-of-Cell Burst Testing, Oak Ridge National Laboratory, ORNL/SPR-2021/2122, 2021.

[33] V. Di Marcello, A. Schubert, J. van de Laar, P. Van Uffelen, The TRANSURANUS mechanical model for large strain analysis, Nucl. Eng. Des. 276 (2014) 19–29. https://doi.org/10.1016/j.nucengdes.2014.04.041.

[34] R.H. Chapman, Multirod Burst Test Program progress report, July--December 1977. [BWR; PWR], Oak Ridge National Laboratory, ORNL/NUREG/TM-200, 1978.

[35] M. Considère, Memoire sur l'emploi du fer et de l'acier dans les constructions," in Annales des Ponts et Chausées, Annales des Ponts et Chausées. 9 (1885) 574–605.

[36] H.W. Swift, Plastic instability under plane stress, J. Mech. Phys. Solids. 1 (1952) 1–18. https://doi.org/10.1016/0022-5096(52)90002-1.